Effects of technological voids and hydration time on the hydro-mechanical behaviour of compacted bentonite/claystone mixture

Zhixiong Zeng, Yu-Jun Cui, Nathalie Conil, Jean Talandier

Effects of technological voids and hydration time on the hydro-mechanical behaviour of compacted bentonite/claystone mixture

Zhixiong Zeng[1*], Yu-Jun Cui[1], Nathalie Conil[2], Jean Talandier[3]

1: Laboratoire Navier/CERMES, Ecole des Ponts ParisTech, 6 et 8 avenue Blaise Pascal, 77455 Marne La Vallée cedex 2, France
2: Andra, Centre de Meuse/Haute-Marne, RD 960, 55290 Bure, France
3: Andra, 1/7, rue Jean Monnet, 92298 Châtenay-Malabry cedex, France

***Corresponding author**

Zhixiong Zeng

Ecole des Ponts ParisTech
6–8 av. Blaise Pascal, Cité Descartes, Champs-sur-Marne
77455 Marne–la–Vallée cedex 2
France
Tel.: +33 781926608
Fax: +33 164153562
E-mail address: zhixiong.zeng@enpc.fr

Abstract: Pre-compacted MX80 bentonite/Callovo-Oxfordian (COx) claystone mixture has been considered as a promising sealing/backfilling material in deep geological repository for high-level radioactive waste in France. When the pre-compacted blocks are emplaced in the gallery, technological voids can remain. After the infiltration of groundwater from the host rock, they will swell freely, filling the technological voids and then undergo further hydration under constant-volume conditions. From the perspective of the storage safety, it is essential to understand the effects of technological voids and hydration time on the hydro-mechanical behaviour of such pre-compacted blocks. In this work, a series of infiltration tests at various hydration times were carried out on compacted MX80 bentonite/COx claystone mixture with different technological voids. The evolutions of the swelling pressures in axial and radial directions as well as the hydraulic conductivity were monitored while wetting. After the predetermined hydration times, the dry density, water content and suction at different positions were determined, together with the microstructure investigation using mercury intrusion porosimetry (MIP). It was observed that the soils close to initial voids swelled and filled the initial voids upon contact with water, with significant increases in large-pore and medium-pore void ratios. From the variation of dry density profile with time, compression and swelling zones could be identified: in the compression zone, the soils corresponding to the initial voids were subjected to compression, with decrease in large-pore and medium-pore void ratios over time, whereas in the swelling zone, the soils with a higher dry density than the expected final one underwent further swelling, with large-pore void ratio increasing untill saturation and then a slight decrease due to the water redistribution in the soil. Due to the soil density heterogeneity, the axial swelling pressure and hydraulic conductivity of samples with voids were slightly larger than those of samples without voids; contrarily, the radial swelling pressure was lower than that of the samples without voids.

Keywords: expansive soils; fabric/structure of soils; time dependence; laboratory tests; radioactive waste disposal

1 Introduction

Many European concepts of deep geological disposal for radioactive waste involve a multi-barrier system consisting of canisters, natural geological barrier (host rock), concrete lining and sealing/backfilling elements. In most cases, compacted blocks manufactured by uniaxial compaction are placed between host rock and canisters, and inevitably, technological voids remain among the blocks, between blocks and canisters and between blocks and host rock (Villar and Lloret, 2008; Wang et al., 2013a; Bian et al., 2019a). These technological voids are estimated at 6.6, 12 and 14% of the total volume of the galleries in the Febex mock-up test (Martin et al., 2006), PGZ2 in situ tests in the underground research laboratory (URL) at Bure (Gatabin et al., 2016) and Sealex in situ test (Wang et al., 2013a; Saba et al., 2014a), respectively. Upon the intrusion of groundwater from the host rock, compacted blocks will swell and fill up the technological voids, closing the preferential pathways (Villar and Lloret, 2008). After that, their swelling will occur under constant-volume conditions. In the long term, they are expected to exhibit a swelling pressure high enough to limit the convergence of the galleries after the failure of concrete lining (Cuisinier et al., 2008) and a hydraulic conductivity low enough to retard the water transfer-related phenomena (Castellanos et al., 2008). Hence, it is essential to well understand thoroughly the hydro-mechanical behaviour of the bentonite-based materials in the assessment of overall repository safety, when technological voids are present.

A number of studies were performed to investigate the effect of technological voids on the hydro-mechanical behaviour of compacted sealing/backfilling materials both in the laboratory and at field scale (Villar et al., 2005; Gens et al., 2011; Wang et al., 2013a; Saba et al., 2014b; 2014c; Mokni et al., 2016; Bian et al., 2019b; Jia et al., 2019). Once the hydration has started, a quick reduction of the dry density of compacted blocks close to the technological voids occurs, leading to a heterogeneous distribution of dry density, with lower dry densities in the area affected by water and higher dry densities in the innermost area (Villar and Lloret, 2008). Bian et al. (2019b) divided the heterogeneous samples into two zones according to the expected final dry density: a compression zone where the dry density was lower than the expected final value and a swelling zone in which the dry density was larger than the expected final value. Over time, the swelling zone would undergo further swelling while the compression zone would be compressed by the swelling pressure. As a result, the dry density gradient would decrease and approach a relatively homogeneous state (Bian et al., 2019b). It was also found that the samples with voids exhibited a hydraulic conductivity of one order of magnitude larger than those

without voids after about 40 h of water hydration. By contrast, the swelling pressure was mainly governed by the expected final dry density, irrespective of the heterogeneity when 14% technological voids were considered (Wang et al., 2013a; Saba et al., 2014b). To the authors' knowledge, the evolutions of the swelling pressures in various directions and hydraulic conductivity of the compacted blocks with technological voids over a long time period have not been comprehensively studied.

Basically, the macroscopic hydro-mechanical response of compacted blocks is directly related to their microstructure changes (Wang et al., 2014; Bian et al., 2019b). Bian et al. (2019b) conducted seven infiltration tests on compacted bentonite with initial voids and investigated the microstructure change with time using mercury intrusion porosimetry (MIP), together with the determination of dry density, water content and suction. They found that the variation of dry density at different positions was well correlated with the microstructure changes, but their work was limited to the microstructural changes of compacted bentonite during the saturation process only. After the full saturation of the compacted blocks, the water exchanges between intra-aggregate and inter-aggregate pores would continue, resulting in a decrease in inter-aggregate porosity and an increase in interlayer porosity due to more water infiltration into the interlayer space inside the aggregates (Delage et al., 2006; Wang et al., 2014). However, it should be pointed out that, although the ageing effect on the microstructure of compacted blocks was identified in several studies, there has been no investigation into the evolution of microstructure with the presence of technological voids over long time period.

In the present study, a series of infiltration tests were carried out on a compacted MX80 bentonite and Callovo-Oxfordian (COx) claystone mixture at different times. The evolutions of swelling pressure and hydraulic conductivity of compacted blocks with different technological voids were evaluated. Moreover, the dry density, water content, suction and microstructure features at different positions after different times were determined, enabling interpretation of the hydro-mechanical behaviour of the compacted mixture with the presence of technological voids.

2 Materials and methods

2.1 Materials

The soil studied is a mixture of MX80 bentonite and COx claystone with a proportion of 30/70 in dry mass, which has been considered as a promising sealing/backfilling material by the

French National Radioactive Waste Management Agency (Andra). The bentonite is a commercial bentonite from Wyoming, USA and its physical and chemical properties are summarized in Table 1. The COx claystone was obtained at about 490 m depth from the Andra URL at Bure, France. The claystone consists of 40-45% clay minerals with predominance of interstratified illite/smectite, 30% carbonates and 25-30% quartz and feldspar (Fouché et al., 2004). It has a liquid limit of 41%, a plastic limit of 24% and an average specific gravity of 2.70. The bentonite and claystone were obtained as granulated powders at water contents of 11.4 and 6.1%, respectively. The grain size distribution curves of MX80 bentonite and COx claystone determined by dry sieving and sedimentation are displayed in Fig. 1. The size of bentonite grains determined by dry sieving was very close to that of claystone grains. Once deflocculated in water, the clay-size fractions (< 2 μm) were determined, and were equal to 86 and 26% for bentonite and claystone, respectively (Zeng et al., 2020a).

Table 1. Physical and chemical properties of MX80 bentonite (the CEC data compiled from Kiviranta and Kumpulainen (2011))

Soil property	Description
Specific gravity	2.76
Consistency limit	
Liquid limit (%)	496
Plastic limit (%)	46
Plasticity index (%)	448
Cation exchange capacity (CEC) (meq/100 g)	84
Main exchange capacity (meq/100 g)	
Na^+	58
K^+	2
Mg^{2+}	8
Ca^{2+}	25
Main minerals	
Montmorillonite (%)	86
Quartz (%)	7

Synthetic water, which has the same chemical composition as the site water, was used for hydration. It was prepared by mixing the chemical components with de-ionised water, according to the recipe shown in Table 2 (Zeng et al., 2019). Note that even though this recipe was different that of Wang et al. (2013b), the ion compositions of the synthetic water prepared according to the two recipes were quite close.

2.2 Experimental set-up

Fig. 2 presents the experimental set-up used in this study. It consists of a stainless cell of dia. 50 mm. The test sample was installed between two porous stones and filter papers. The sample

was saturated from the bottom and the constant-volume condition was ensured by the stainless cell and a top piston, which was fixed with a screw. A force transducer under the cell and a total pressure sensor in the cell were installed for the axial and radial pressure measurements, respectively.

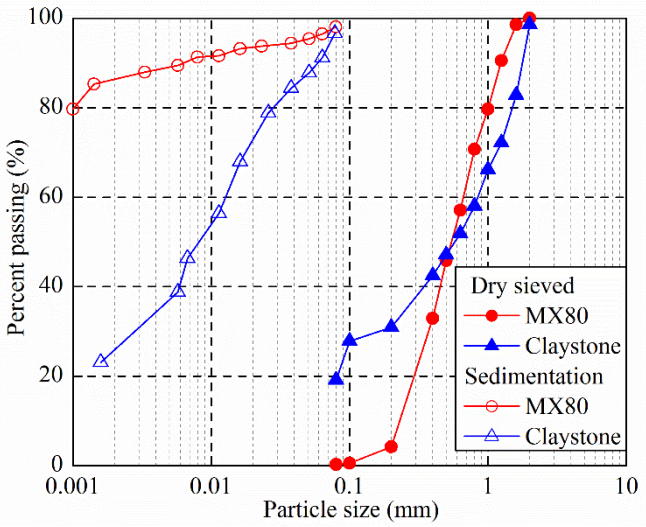

Fig. 1. Grain size distribution of MX80 bentonite and crushed COx claystone (Zeng et al., 2020a)

Table 2. Recipe for the synthetic water preparation

Component	NaCl	$NaHCO_3$	KCl	$CaSO_4$·$2H_2O$	$MgSO_4$·$7H_2O$	$CaCl_2$·$2H_2O$	Na_2SO_4
Content (g/L)	1.950	0.130	0.035	0.630	1.020	0.080	0.700

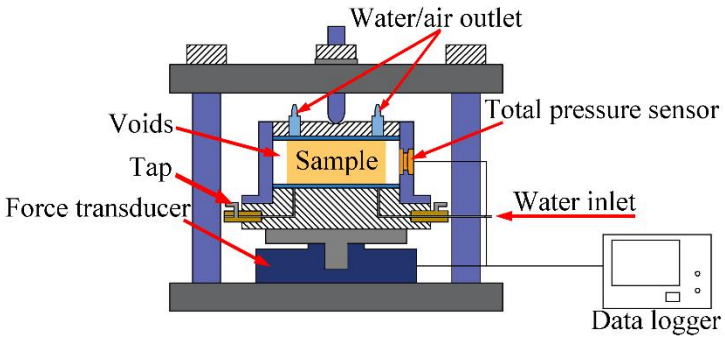

Fig. 2. Layout of the constant-volume cell for swelling pressure and hydraulic conductivity tests

2.3 Sample preparation and test procedure

The bentonite and claystone powders (30% bentonite - 70% claystone in dry mass) were carefully mixed for more than 10 min to obtain a relatively homogeneous state. The obtained mixture had a water content of 7.7%. Next, a predetermined amount of mixture was poured into a rigid ring (50 mm in dia.) and statically compacted at a controlled displacement rate of 0.05 mm/min. The target height of samples was 10 mm and the dry densities were 1.6, 1.8 and 2.0 Mg/m^3 (Table 3).

To study the effect of technological voids, 14 samples (T01 to T14) with a dry density of 2.0 Mg/m^3 were trimmed to different diameters of 47.43 and 44.72 mm (Fig. 3). When the samples were installed and centered in the cell, there were initial voids between the samples and the inner wall of cell, corresponding to 10 and 20% of the total volume for the samples with diameters of 47.43 and 44.72 mm, respectively. Before hydration, an initial axial pressure of 0.05 MPa was applied onto the samples to ensure good contact. For each case, seven identical samples were prepared and hydrated using synthetic water for 0.5, 5, 15, 60, 240, 720 and 2160 h to study the time effect. The expected final dry densities were 1.8 and 1.6 Mg/m^3 for the samples with initial diameters of 47.43 and 44.72 mm, respectively. For comparison, three 50 mm dia. samples with dry densities of 1.6, 1.8 and 2.0 Mg/m^3 (T15 to T17) were hydrated with synthetic water for 2160 h. The evolutions of both axial and radial pressures were determined during hydration. For the tests with less than 60 h of hydration (T01 to T04 and T08 to T11), the samples were hydrated using a Pressure/Volume controller to record the volume of injected synthetic water. For the tests with more than 240-h hydration (T05 to T07 and T12 to T17), the samples were first hydrated under a water head of about 1 m until the predetermined hydration times (see Table 3). After that, the synthetic water injection was continued using a Pressure/Volume controller under constant pressures of 0.04, 0.1 and 0.2 MPa (less than 1/10 of the swelling pressure) for the samples with expected final dry densities of 1.6, 1.8 and 2.0 Mg/m^3, respectively.

After the infiltration tests, the samples with initial technological voids were carefully taken out of the test cell by slowly pushing the sample from the bottom to minimise soil disturbance. Then, they were divided into three parts, namely part I, part II and part III, as shown in Fig. 4. Part I, including the initial voids, referred to a ring with inner and outer diameters of 40 and 50 mm. Part II corresponded to a ring with inner and outer diameters of 20 and 40 mm and the rest of cylinder with a diameter of 20 mm belonged to part III. Each part was cut into several pieces for the determination of water content, dry density and suction as well as the microstructural investigation. The water content of soils was determined by oven-drying at 105°C for a period of 24 h and the soil volume was determined by hydrostatic weighing after immersing the soil into a non-aromatic hydrocarbon fluid (Kerdane) (Bian et al., 2019b). The suction was measured with a chilled mirror dew point tensiometer (Decagon WP4). The microstructure was determined using the MIP technique. To ensure the quality of microstructure investigation, the samples (about 1.5 g) were first freeze-dried prior to MIP testing. The applied pressure ranged from 3.6×10^{-3} to 228 MPa, allowing the exploration of pore diameters from 350 to 0.006 μm.

Table 3. Experimental programme

Test	Technological voids (%)	Duration (h)	Initial dry density of block (Mg/m^3)	Expected final dry density (Mg/m^3)	MIP
T01	20	0.5	2.0	1.6	√
T02	20	5	2.0	1.6	√
T03	20	15	2.0	1.6	√
T04	20	60	2.0	1.6	√
T05	20	240	2.0	1.6	√
T06	20	720	2.0	1.6	√
T07	20	2160	2.0	1.6	√
T08	10	0.5	2.0	1.8	√
T09	10	5	2.0	1.8	√
T10	10	15	2.0	1.8	√
T11	10	60	2.0	1.8	√
T12	10	240	2.0	1.8	√
T13	10	720	2.0	1.8	√
T14	10	2160	2.0	1.8	√
T15	0	2160	2.0	2.0	-
T16	0	2160	1.8	1.8	-
T17	0	2160	1.6	1.6	-

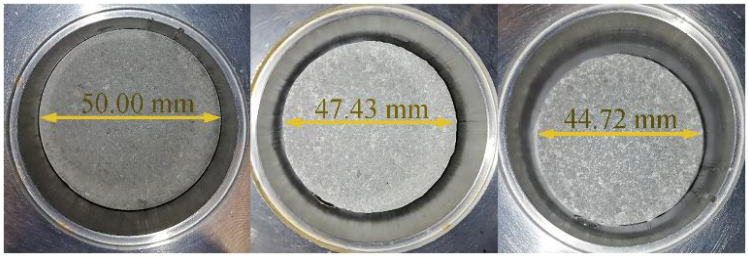

Fig. 3. Preparation of samples with and without voids

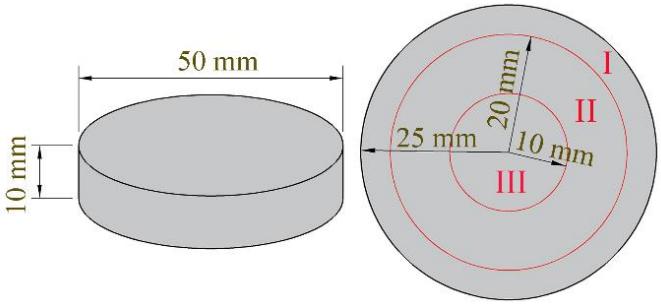

Fig. 4. Schematic view of the sample cutting

3 Experimental results

3.1 Axial and radial swelling pressures

As the hydration started, the synthetic water would fill up the technological voids and infiltrate into the compacted block from top, bottom and lateral sides. The compacted block was under a

free-swell condition in the radial direction and a confined condition in the axial direction. Fig. 5 depicts the evolution of axial swelling pressure of samples with different technological voids over various times. It clearly shows that the curves of identical samples for different hydration times were quite close, indicating a good repeatability of the infiltration tests. For test T15 without voids, the axial swelling pressure increased rapidly and then tended to stabilisation at 58.3 h (Fig. 5a). For the samples with 10% voids (T08 to T14), the axial swelling pressure started with a quick increase and reached stabilisation after 7.4 h (Fig. 5b). For the samples with 20% voids (T01 to T07), the swelling pressure increased at the beginning of hydration, reaching a peak value of 0.80 MPa at 0.68 h. Then, it decreased to about 0.57 MPa at 5.8 h and tended to stabilise (Fig. 5c). The occurrence of peaks could be attributed to the fact that the radial swelling of compacted block would decrease the dry density of compacted block and reduce the axial pressure. When the reduction of axial pressure due to the radial swelling was larger than the increase of axial swelling, the peaks appeared. The final axial swelling pressures after 2160-h hydration were 1.63 and 0.53 MPa for the samples with 10 and 20% technological voids, respectively. The larger the technological voids, the lower the final axial swelling pressure.

The evolution of radial swelling pressure with respect to elapsed time for all the samples is shown in Fig. 6. For test T15 without voids, the radial swelling pressure increased rapidly and then reached stabilisation after 54.0 h (Fig. 6a). For the samples with voids (T01 to T14), the radial pressure kept zero at the beginning of hydration. With further radial swelling, the soils came in contact with the sensor, and the radial swelling pressures became detectable after 0.08 and 0.18 h for the samples with 10 and 20% voids. Afterwards, they increased and then tended to stabilise after 7.5 and 5.7 h, respectively (Fig. 6b and c). The final radial swelling pressure decreased with the increase of technological voids.

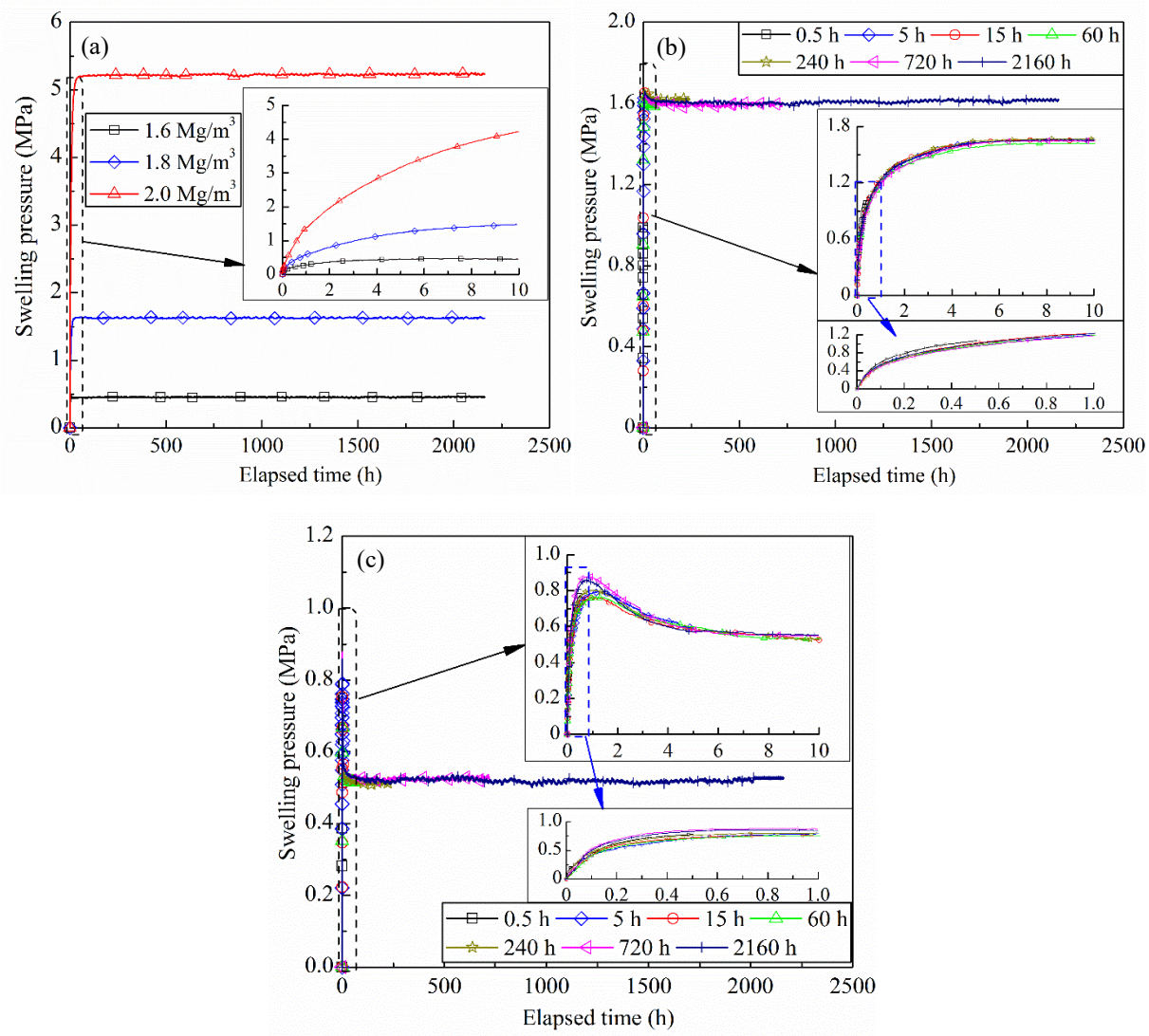

Fig. 5. Evolution of axial swelling pressure of samples: (a) without voids; (b) with 10% voids; (c) with 20% voids

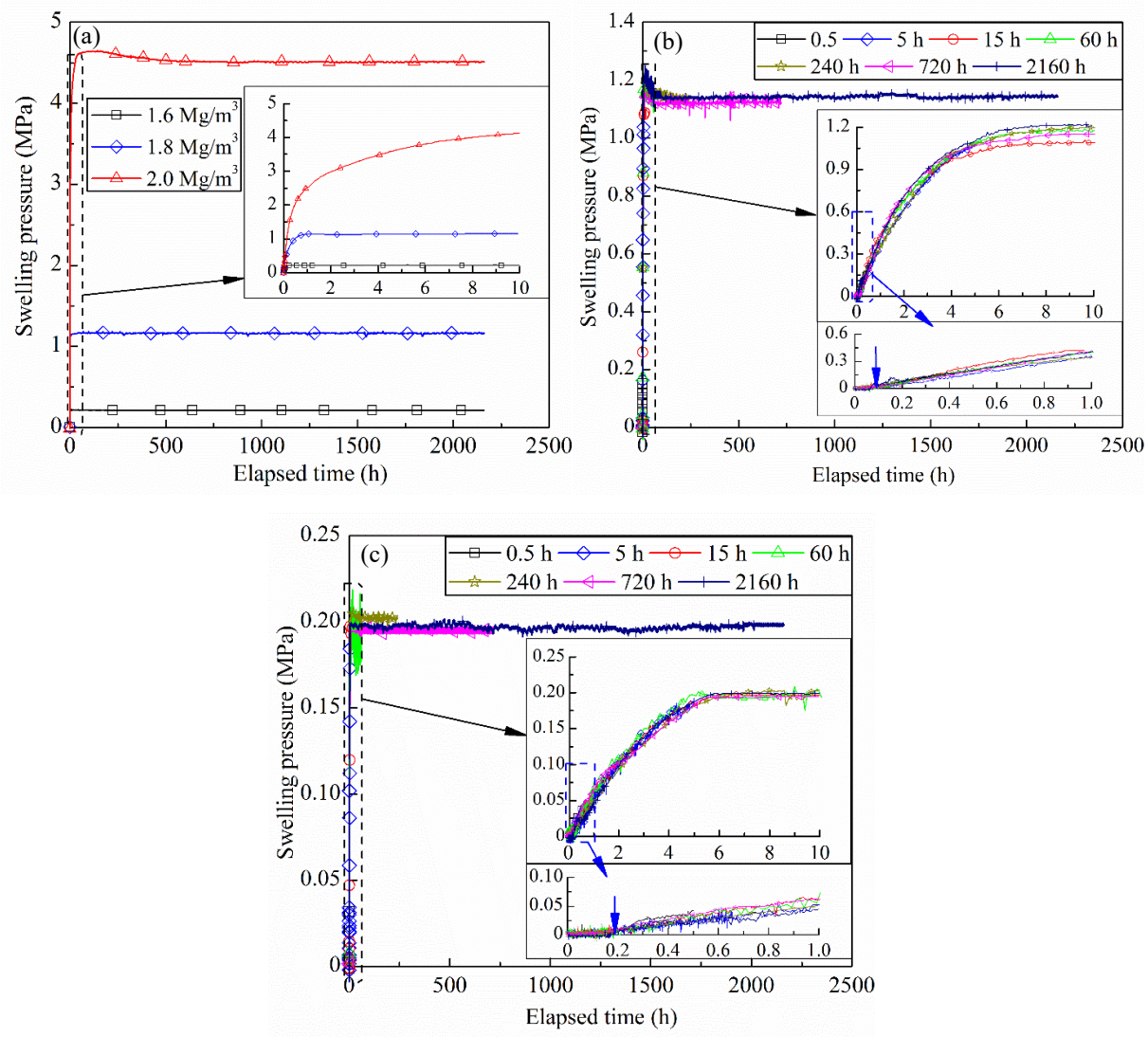

Fig. 6. Evolution of radial swelling pressure of samples: (a) without voids; (b) with 10% voids; (c) with 20% voids

3.2 Hydraulic conductivity

The theoretical water volumes required for saturating the samples (3.91 and 5.66 cm^3 for the samples with 10 and 20% voids, respectively) were lower than one-tenth of the total volumes of injected synthetic water after 5 h (78.05 and 87.27 cm^3 for the samples with 10 and 20% voids, respectively). Therefore, the hydraulic conductivity was determined according to the variation of synthetic water inflow recorded by the pressure/volume controller, without considering the synthetic water volume for saturating the samples. The evolutions of calculated hydraulic conductivities of samples with initial voids are presented in Fig. 7. Overall, a bi-linear decrease of hydraulic conductivity was clearly identified with the elapsed time in spite of the data scatter. A critical time could be thus defined: the slope before the critical time was noticeably larger than that after the critical time. The values of 7.5 and 5.8 h could be determined

at the intersection of two lines for the samples with 10 and 20% voids, respectively. Note that these critical times were very close to those required to reach stabilisation of the axial and radial swelling pressures, indicating a good compatibility between the hydraulic and mechanical parameters. It could be suspected that, before the critical times, the technological voids and the subsequent swollen soil with a larger void ratio around the sample governed the synthetic water flow. The progressively increasing radial swelling pressure compressed the swollen soil gradually and led to a decrease in hydraulic conductivity. By contrast, after the critical times, the swollen soil was subjected to consolidation under almost constant pressure and the hydraulic conductivity was decreasing but at a lower decreasing rate. As far as the final hydraulic conductivity was concerned, the final values of the samples without voids were 6.94×10^{-13}, 2.12×10^{-12} and 1.11×10^{-11} m/s for dry densities of 2.0, 1.8 and 1.6 Mg/m^3, respectively, while slightly higher hydraulic conductivities of 2.32×10^{-12} and 1.19×10^{-11} m/s were observed for the samples with 10 and 20% voids (corresponding to the expected final dry densities of 1.8 and 1.6 Mg/m^3, respectively).

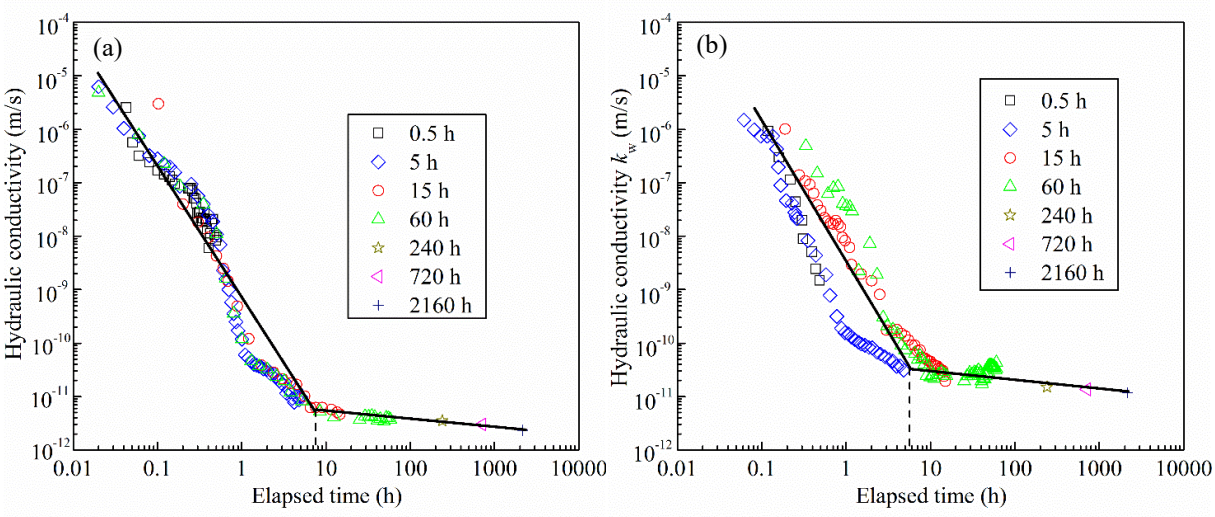

Fig. 7. Evolutions of hydraulic conductivities of samples: (a) with 10% voids; (b) with 20% voids

3.3 Water content, dry density and suction profiles

The water content and dry density profiles of the samples at different hydration times are depicted in Figs. 8 and 9. The water content and dry density exhibited rather heterogeneous distributions, with a higher water content and a lower dry density for part I, which included the initial voids. With the decrease of the distance from the center, the water content decreased and the dry density increased. Over time, the water content of part I including initial voids decreased while those of parts II and III far from the initial voids increased, leading to a decrease in water content gradient (Fig. 8). By contrast, the dry density of part I increased while those of parts II

and III decreased with time, approaching the expected final dry density (Fig. 9). Further examination of the evolutions of water content and dry density profiles showed a larger variation rate during the first 5 h but a lower one after 15 h, which was consistent with the phenomenon observed in the evolution of hydraulic conductivity. The dramatic decrease of dry density of part II and III especially during the first 5 h for the samples with 20% voids confirmed that the peak occurrence on the axial swelling pressure curve was related to the swelling of compacted block in the radial direction. Additionally, according to the measured water content and dry density, the degree of saturation of each part was calculated by considering a water density of 1.0 Mg/m^3 and the calculated results are summarized in Fig. 10. For part I, the degree of saturation quickly increased from 58% to larger than 98% after 0.5 h. By contrast, the degree of saturation of parts II and III increased during the first 5 h of hydration and then kept within the range of 98 to 102%.

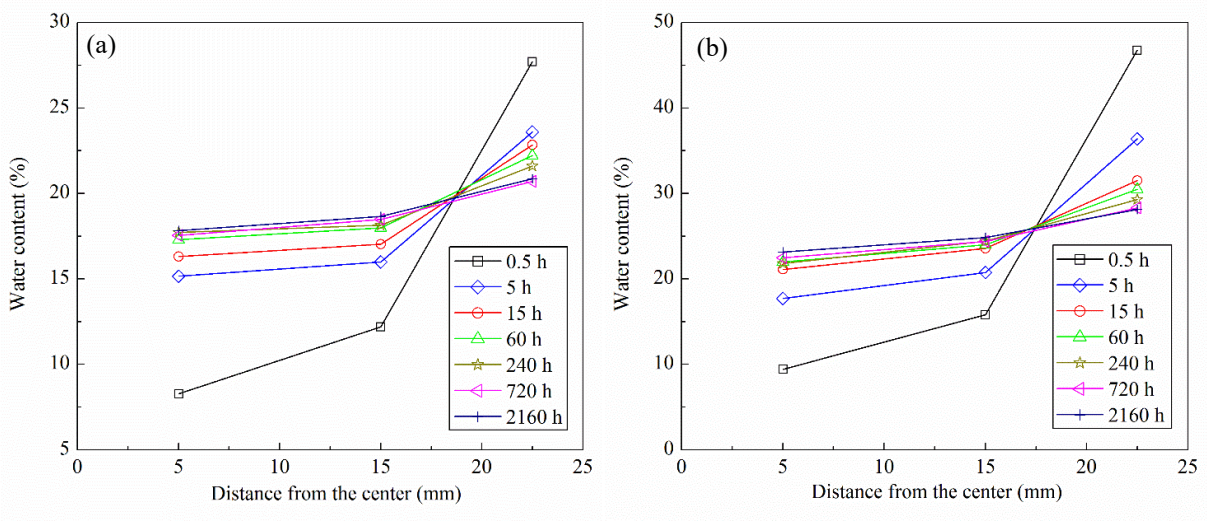

Fig. 8. Water content profiles after tests: (a) with 10% voids; (b) with 20% voids

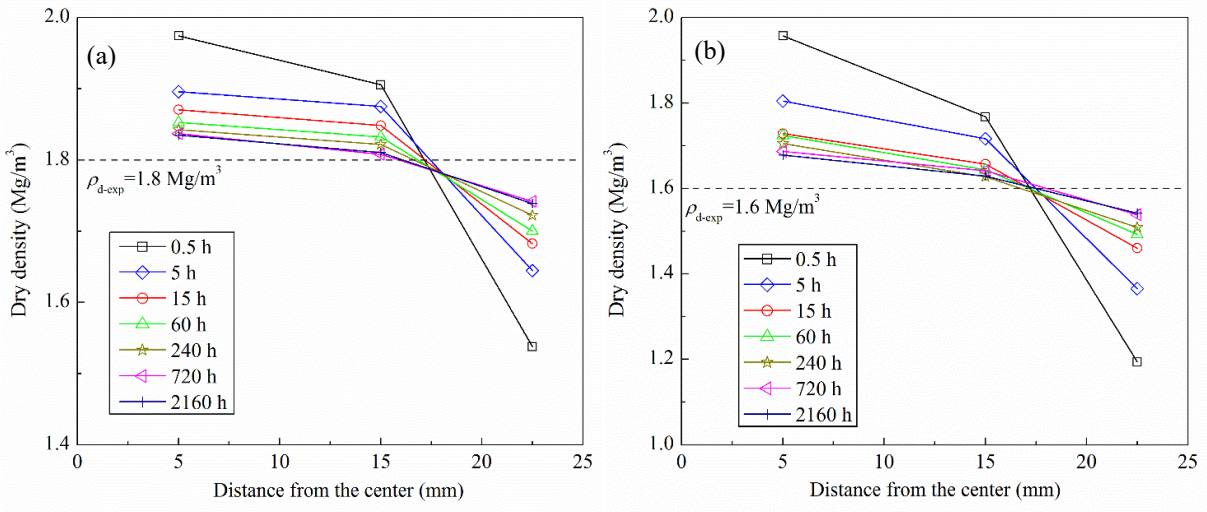

Fig. 9. Dry density profiles after tests: (a) with 10% voids; (b) with 20% voids

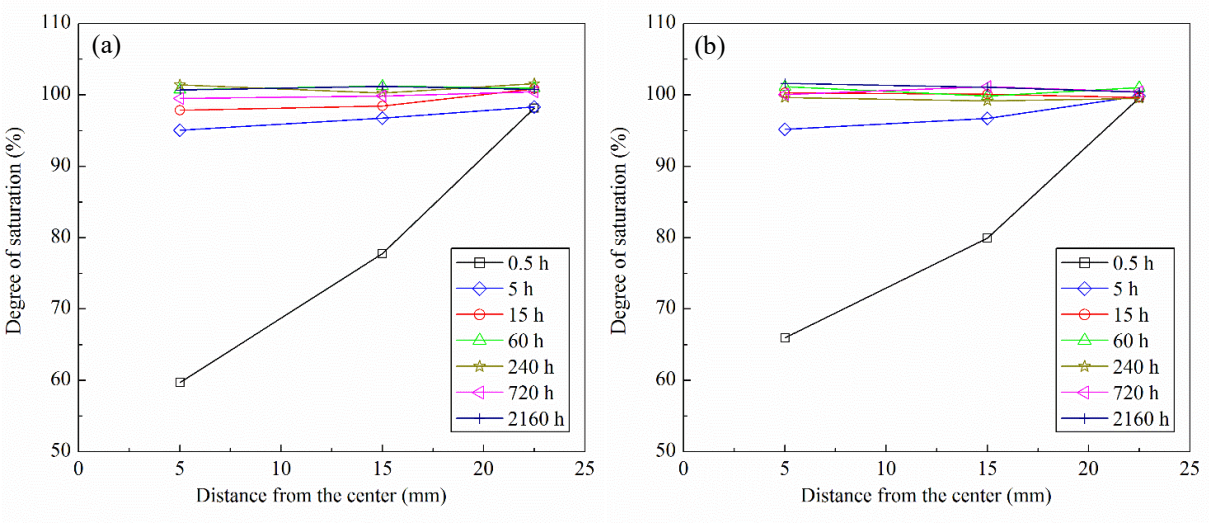

Fig. 10. Degree of saturation profiles after tests: (a) with 10% voids; (b) with 20% voids

The variation of suction profile with time for samples with technological voids is presented in Fig. 11. A drastic decrease of suction from 74.3 MPa at the as-compacted state to below 1.0 MPa after 0.5 h of hydration could be observed for part I, which included initial voids. The suction decrease was much less significant for parts II and III. For the samples with 10% voids, the suctions of parts II and III decreased to 1.50 and 1.38 MPa at 5 h, respectively (Fig. 11a), whereas the suctions of parts II and III for the samples with 20% voids decreased to 1.00 and 1.06 MPa at 5 h, respectively (Fig. 11b). Afterwards, the suctions of parts II and III went down below 1.0 MPa and reached stabilisation after 15 h.

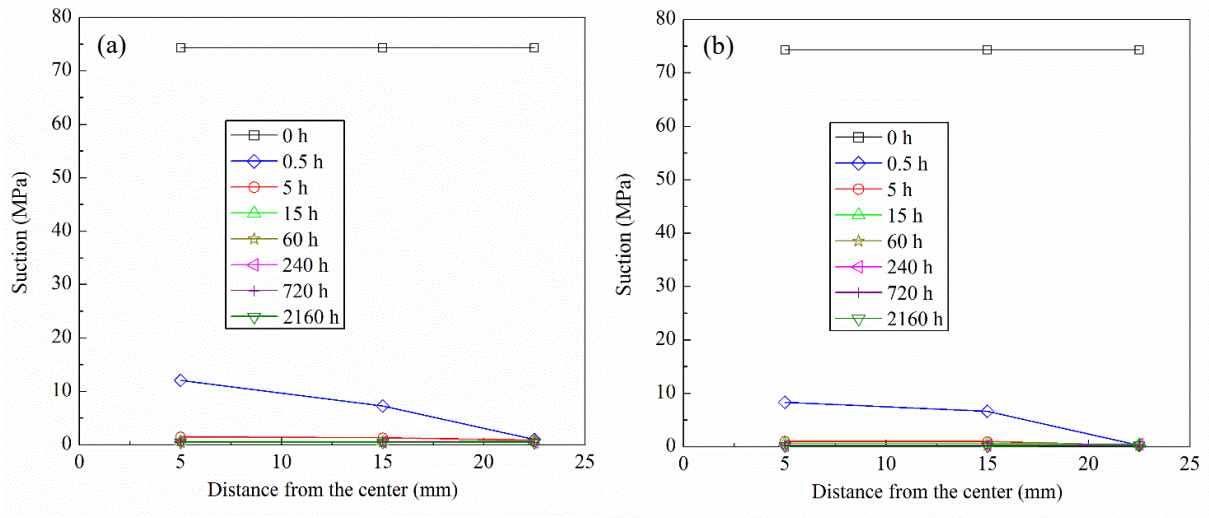

Fig. 11. Suction profiles before and after tests: (a) with 10% voids; (b) with 20% voids

3.4 Microstructure distribution

Figs. 12 and 13 present the pore size distribution of the samples with 10 and 20% voids, respectively, together with that of the as-compacted sample at a dry density of 2.0 Mg/m^3. For

the samples with technological voids, the cumulative curves of part I at a longer time lied below those at a shorter time while the cumulative curves of parts II and III at a longer time lied above those at a shorter time (Figs. 12 and 13). A comparison between different parts showed that the total cumulative curves along the y-axis were distributed in the following order: parts I, II and III, the same order as the increasing dry density. Moreover, the difference between different parts decreased with time. For all the curves, it could be observed that the final value of intruded mercury volume was lower than the soil void ratio. This phenomenon was due to the limited range of the pressure applied in the MIP tests. Some pores with a size smaller than 0.006 μm or larger than 350 μm could not be determined and they were termed as 'inaccessible-pores' in further analysis.

Regarding the density function curves, a typical bimodal porosity for the as-compacted sample with a dry density of 2.0 Mg/m^3 was observed: inter-aggregate pores with a mean pore size of 5 μm and intra-aggregate pores with a mean pore size of 0.02 μm. After hydration, in addition to the two main populations for the as-compacted sample, a new pore population ranging from 0.04 to 2 μm was formed (Figs. 12 and 13). Following the suggestion of Wang et al. (2014) and Bian et al. (2019b), four pore populations were defined: inaccessible-pores (< 0.006 μm and > 350 μm), small-pores (0.006-0.04 μm), medium-pores (0.04-2 μm) and large-pores (2-350 μm). Over time, the medium-pore size of part I decreased, whereas those of parts II and III increased. The large-pore size of part I decreased, while those of parts II and III increased during the first 5 h of hydration and then decreased slightly after 15 h. Consequently, the microstructure of parts I, II and III approached a relatively uniform state. Additionally, the void ratio of each pore population at different times was calculated and the variations of the void ratios corresponding to the four pore populations with time are shown in Figs. 14 and 15. For the samples with technological voids, the large-pore and medium-pore void ratios of part I decreased with time after an initial strong increase, while the inaccessible-pore void ratio increased slightly, without significant changes in small-pore void ratio. For parts II and III, the medium-pore and inaccessible-pore void ratios increased with hydration time while the small-pore void ratio decreased. The larger-pore void ratio of parts II and III increased during the first 5 h of hydration and then started to decrease after 15 h. A comparison between the different parts showed that larger inaccessible-pore, medium-pore and large-pore void ratios and a lower small-pore void ratio were observed for part I, which included initial technological voids.

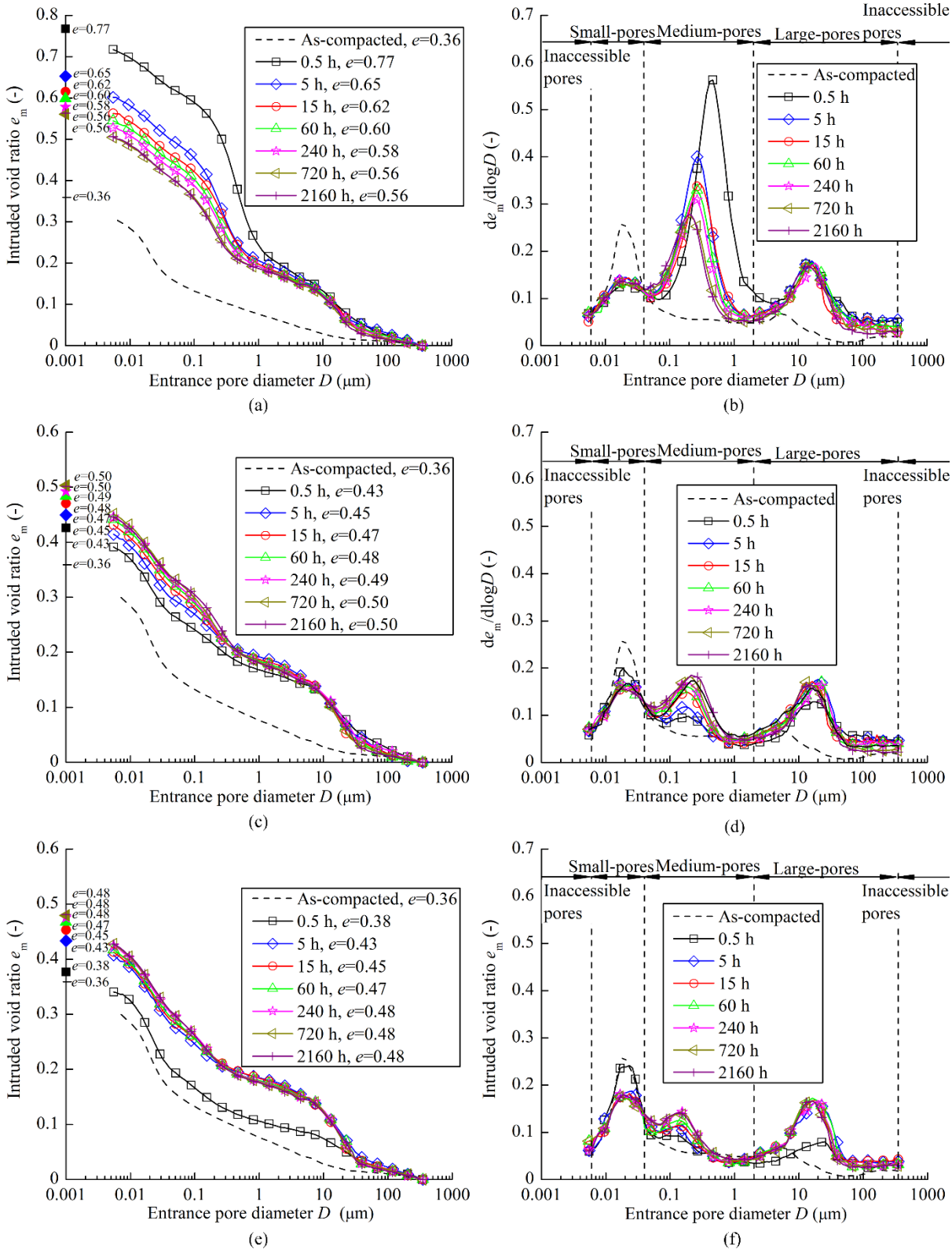

Fig. 12. Pore size distribution of different parts for the samples with 10% voids: (a) cumulative curves of part I; (b) density function curves of part I; (c) cumulative curves of part II; (d) density function curves of part II; (e) cumulative curves of part III; (f) density function curves of part III

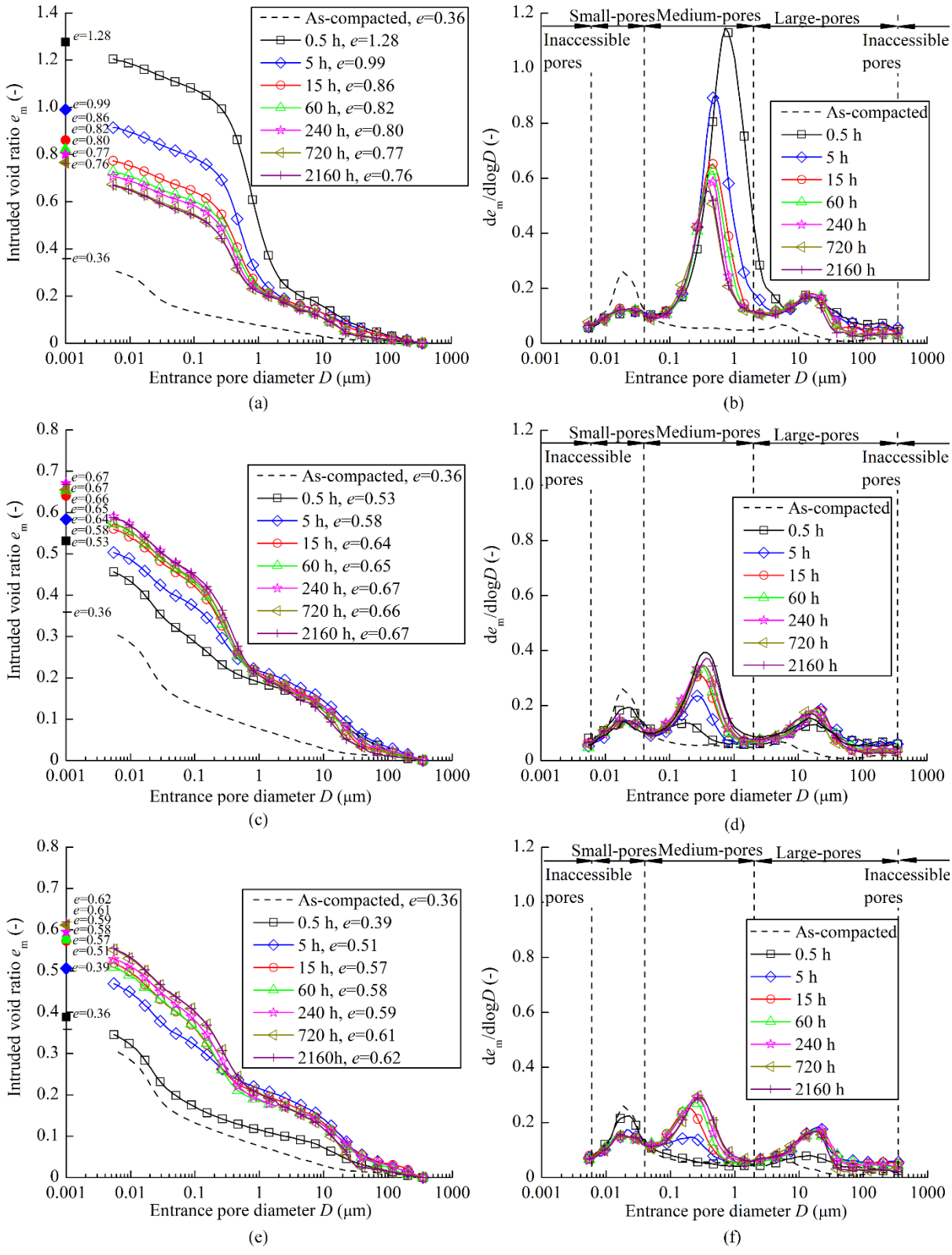

Fig. 13. Pore size distribution of different parts for the samples with 20% voids: (a) cumulative curves of part I; (b) density function curves of part I; (c) cumulative curves of part II; (d) density function curves of part II; (e) cumulative curves of part III; (f) density function curves of part III

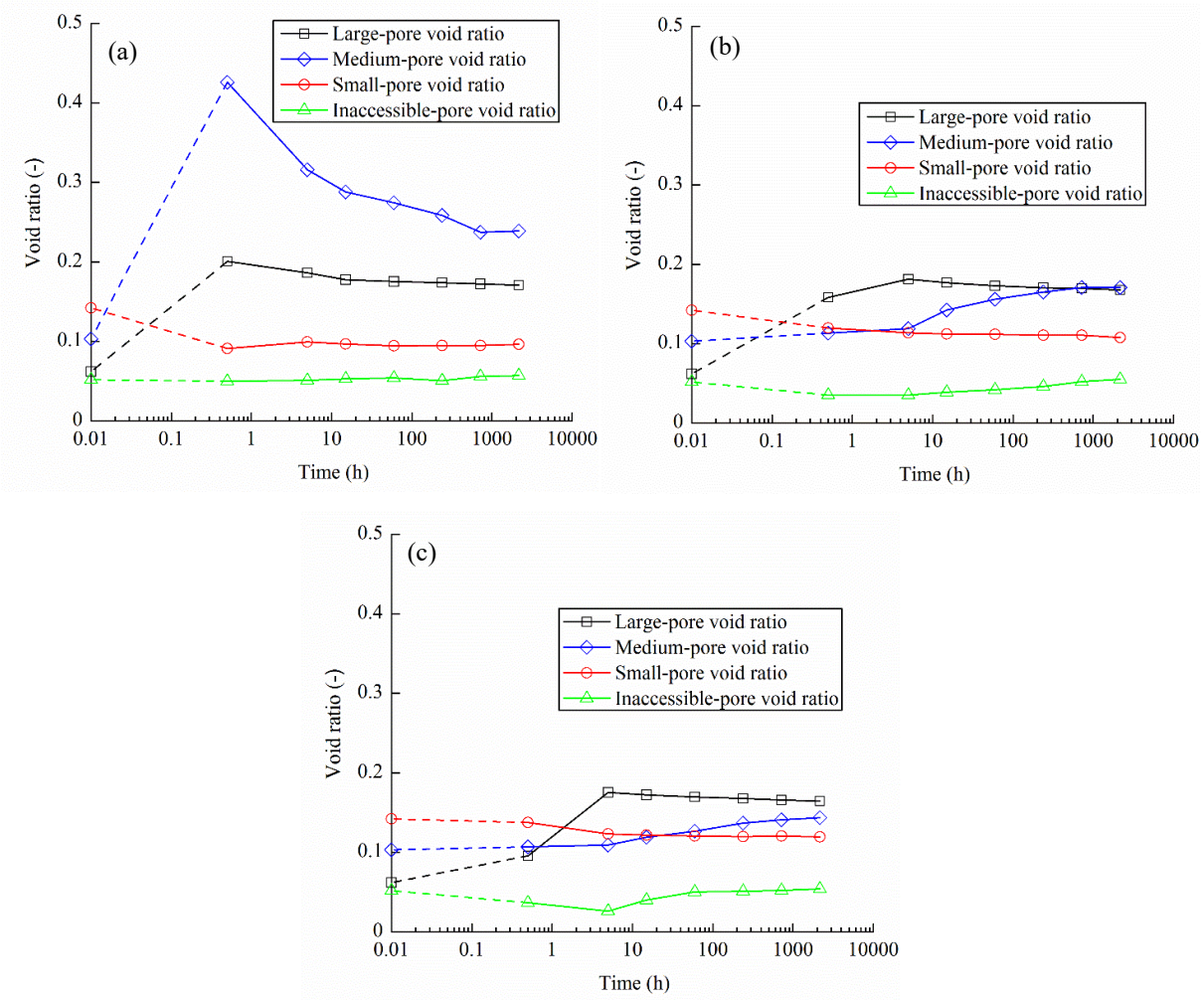

Fig. 14. Changes in inaccessible-pore, small-pore, medium-pore and large-pore void ratios with time for the samples with 10% voids: (a) part I; (b) part II; (c) part III

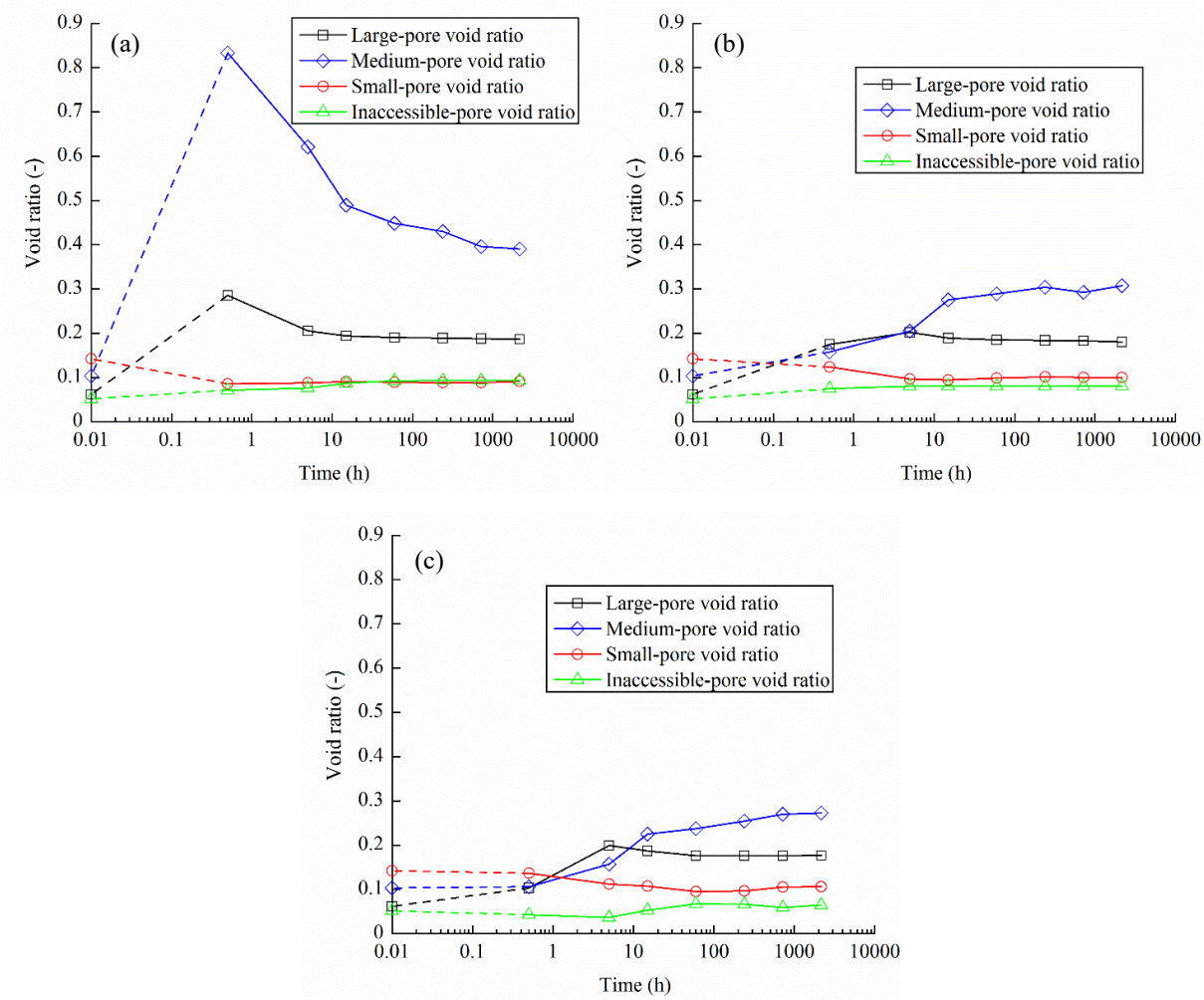

Fig. 15. Changes in inaccessible-pore, small-pore, medium-pore and large-pore void ratios with time for the samples with 20% voids: (a) part I; (b) part II; (c) part III

4 Discussions

4.1 Swelling behaviour of samples with technological voids

As shown in Fig. 6b and c, the radial swelling pressure of the samples with technological voids started to increase after a certain time. This phenomenon implied two stages during the hydration of samples with voids: a filling stage corresponding to the filling up of initial voids by the swollen soil, leading to heterogeneous distributions of water content and dry density; and a homogenization stage corresponding to the decreasing water content and dry density gradients, which allowed the samples to approach a relatively homogeneous state. As noted earlier, the filling stage lasted 0.08 and 0.18 h for the samples with 10 and 20% voids, respectively. After that, the samples could be divided into two zones: compression and swelling zones based on the dry density distribution (Bian et al., 2019b). In this study, parts II and III corresponded to the swelling zone which would undergo further swelling, resulting in a decrease of dry density, whereas part I including the initial voids corresponded to the

compression zone, which would be subjected to compression, leading to an increase of dry density over time. Consequently, the dry density of three parts gradually reached the expected final state over time. For the samples with larger technological voids, a lower swelling pressure was generated and thus a lower homogenization rate was observed (Fig. 9).

4.2 Microstructural mechanism

4.2.1 Compression zone

At the filling stage, the soils adjacent to the voids swelled with a rapid decrease in suction from 74.3 MPa to below 1.0 MPa (Fig. 11). Water molecules were expected to progressively placed on the clay surface, layer by layer up to four layers, with an increase in the inter-layer space, which was inaccessible by the MIP observation (Saiyouri et al., 1998; 2000). During this process, the clay particles could exfoliate upon saturation and form a gel, progressively filling the inter-aggregate pores with a decrease in pore volume (Bian et al., 2020). Moreover, clay aggregates would be divided into thinner particles as the suction was lower than 9.0 MPa, leading to an increase in the intra-aggregate pore size (Cui et al., 2002; Wang et al., 2013b). With the transformations of inter-aggregate and intra-aggregate pores into the medium-pore population, a significant increase in the medium-pore void ratio was observed. Additionally, fissure-like 2-dmensional (2D) pores with a mean pore size of 20 μm appeared, explaining the increased void ratio of large pores (Wang et al., 2014; Zeng et al., 2016). At the homogenization stage, the large pores and medium pores of the compression zone were compressed gradually by the swelling pressure, leading to decreases in large-pore and medium-pore void ratios.

4.2.2 Swelling zone

At the filling stage, the soils inside the compacted block were subjected to slower hydration due to the larger radial distance to the hydration front, as compared to those in the external part, with gradual increases in large-pore and medium-pore void ratios and a decrease in small-pore void ratio. After the filling stage, the water gradually infiltrated into the swelling zone (parts II and III) and the suction of the swelling zone decreased to 1.0-1.5 MPa at 5 h (Fig. 11). The large-pore and medium-pore void ratios increased and the small-pore void ratio decreased significantly due to the further radial swelling of compacted block, especially for the samples with 20% voids, which explained the peak occurrence of axial swelling pressure (Fig. 5c). While reaching saturation at 15 h with suction approaching zero, the soils exhibited a slow swelling, with a slight decrease in dry density. Over time, increases in the medium-pore and inaccessible-pore void ratios and decreases in the large-pore and small-pore void ratios were

observed. This phenomenon could be explained by the water redistribution in the soil (Delage et al., 2006; Ye et al., 2013; Wang et al., 2014). The inter-aggregate pores were first filled due to their high permeability, but the water filling the inter-aggregate pores was not necessarily in equilibrium with that inside the aggregates in terms of water potential (Alonso et al., 2011; Wang et al., 2014). Over time, this water in the inter-aggregate pores was driven to the intra-aggregate pores, leading to further sub-division of the clay particles and filling up of large pores by clay exfoliation. Obviously, this process was soil dry density dependent (Wang et al., 2014). More pronounced microstructure changes after saturation occurred in the swelling zone of the samples with 20% technological voids (Fig. 15).

4.3 Axial and radial swelling pressures

The relationships between the final axial and radial swelling pressures after 2160 h of hydration and the expected final dry density for the samples with and without technological voids are shown in Fig. 16. From Fig. 16a, it appears that there was a unique relationship between the axial swelling pressure (P_a in MPa) and the dry density (ρ_d in Mg/m^3) for the samples without voids:

$$P_a = a_1 \exp^{b_1 \rho_d} = 2.591 \times 10^{-5} \exp^{6.117 \rho_d} \quad (1)$$

where a_1 and b_1 are the fitting parameters. For the samples with 10 and 20% voids, the final axial swelling pressures were 1.63 and 0.53 MPa, respectively, which were slightly larger than those of samples without voids (1.62 and 0.45 MPa for the samples at dry densities of 1.8 and 1.6 Mg/m^3). The higher axial swelling pressure for the sample with voids could be attributed to its significantly heterogeneous distribution of dry density (Fig. 9). According to the cell design, the axial force of samples is transmitted to the piston and then the force transducer (Saba et al., 2014c). Thereby, the measured axial swelling pressure corresponded to the global pressure at the top of samples. From Eq. (1), the axial swelling pressures of parts I, II and III could be estimated and the global axial swelling pressure of samples with voids ($P_{a\text{-void}}$) can be approximated by the arithmetic mean value of three parts, as follows:

$$P_{a\text{-void}} = \frac{A_1 P_{a1} + A_2 P_{a2} + A_3 P_{a3}}{A} = \frac{A_1 a_1 \exp^{b_1 \rho_{d1}} + A_2 a_1 \exp^{b_1 \rho_{d2}} + A_3 a_1 \exp^{b_1 \rho_{d3}}}{A} \quad (2)$$

where P_{a1}, P_{a2} and P_{a3} are the axial swelling pressures of parts I, II and III; ρ_{d1}, ρ_{d2} and ρ_{d3} are the dry densities of parts I, II and III; A_1, A_2 and A_3 are the cross-sectional areas of parts I, II and III, respectively; A is the total cross-sectional area of the samples, equal to the sum of A_1, A_2 and A_3. The relationship between the expected final dry density ($\rho_{d\text{-exp}}$) and the dry densities of the three parts is described using the following expression:

$$\rho_{\text{d-exp}}=\frac{A_1\rho_{\text{d1}}+A_2\rho_{\text{d2}}+A_3\rho_{\text{d3}}}{A} \tag{3}$$

By substituting Eq. (3) into Eq. (2), $P_{\text{a-void}}$ can be rewritten as a function of two variables: ρ_{d1} and ρ_{d2}, as follows:

$$P_{\text{a-void}}=a_1\frac{A_1\exp^{b_1\rho_{\text{d1}}}+A_2\exp^{b_1\rho_{\text{d2}}}+A_3\exp^{b_1(A\rho_{\text{d-exp}}-A_1\rho_{\text{d1}}-A_2\rho_{\text{d2}})/A_3}}{A} \tag{4}$$

To find the critical points of $P_{\text{a-void}}$, the first- and second-order partial derivatives $\partial P_{\text{a-void}}/\partial\rho_{\text{d1}}$, $\partial P_{\text{a-void}}/\partial\rho_{\text{d2}}$, $\partial^2 P_{\text{a-void}}/\partial\rho^2_{\text{d1}}$, $\partial^2 P_{\text{a-void}}/\partial\rho^2_{\text{d1}}$ and $\partial^2 P_{\text{a-void}}/(\partial\rho_{\text{d1}}\partial\rho_{\text{d2}})$ are calculated:

$$\frac{\partial P_{\text{a-void}}}{\partial\rho_{\text{d1}}}=\frac{a_1b_1A_1\exp^{b_1\rho_{\text{d1}}}}{A}-\frac{a_1b_1A_1\exp^{b_1(A\rho_{\text{d-exp}}-A_1\rho_{\text{d1}}-A_2\rho_{\text{d2}})/A_3}}{A} \tag{5}$$

$$\frac{\partial P_{\text{a-void}}}{\partial\rho_{\text{d2}}}=\frac{a_1b_1A_2\exp^{b_1\rho_{\text{d2}}}}{A}-\frac{a_1b_1A_2\exp^{b_1(A\rho_{\text{d-exp}}-A_1\rho_{\text{d1}}-A_2\rho_{\text{d2}})/A_3}}{A} \tag{6}$$

$$\frac{\partial^2 P_{\text{a-void}}}{\partial\rho^2_{\text{d1}}}=\frac{a_1b_1^2A_1\exp^{b_1\rho_{\text{d1}}}}{A}+\frac{a_1b_1^2A_1^2\exp^{b_1(A\rho_{\text{d-exp}}-A_1\rho_{\text{d1}}-A_2\rho_{\text{d2}})/A_3}}{AA_3} \tag{7}$$

$$\frac{\partial^2 P_{\text{a-void}}}{\partial\rho^2_{\text{d2}}}=\frac{a_1b_1^2A_2\exp^{b_1\rho_{\text{d2}}}}{A}+\frac{a_1b_1^2A_2^2\exp^{b_1(A\rho_{\text{d-exp}}-A_1\rho_{\text{d1}}-A_2\rho_{\text{d2}})/A_3}}{AA_3} \tag{8}$$

$$\frac{\partial^2 P_{\text{a-void}}}{\partial\rho_{\text{d1}}\partial\rho_{\text{d2}}}=\frac{a_1b_1^2A_1A_2\exp^{b_1(A\rho_{\text{d-exp}}-A_1\rho_{\text{d1}}-A_2\rho_{\text{d2}})/A_3}}{AA_3} \tag{9}$$

Setting both $\partial P_{\text{a-void}}/\partial\rho_{\text{d1}}$ and $\partial P_{\text{a-void}}/\partial\rho_{\text{d2}}$ equal to zero yields:

$$\begin{cases}\dfrac{\partial P_{\text{a-void}}}{\partial\rho_{\text{d1}}}=\dfrac{a_1b_1A_1\exp^{b_1\rho_{\text{d1}}}}{A}-\dfrac{a_1b_1A_1\exp^{b_1(A\rho_{\text{d-exp}}-A_1\rho_{\text{d1}}-A_2\rho_{\text{d2}})/A_3}}{A}=0\\ \dfrac{\partial P_{\text{a-void}}}{\partial\rho_{\text{d2}}}=\dfrac{a_1b_1A_2\exp^{b_1\rho_{\text{d2}}}}{A}-\dfrac{a_1b_1A_2\exp^{b_1(A\rho_{\text{d-exp}}-A_1\rho_{\text{d1}}-A_2\rho_{\text{d2}})/A_3}}{A}=0\end{cases} \tag{10}$$

In Eq. (10), $\rho_{\text{d1}}=\rho_{\text{d-exp}}$ and $\rho_{\text{d2}}=\rho_{\text{d-exp}}$; thus, $(\rho_{\text{d-exp}}, \rho_{\text{d-exp}})$ is a critical point of $P_{\text{a-void}}$.

$$\left[\frac{\partial^2 P_{\text{a-void}}}{\partial\rho^2_{\text{d1}}}(\rho_{\text{d-exp}},\rho_{\text{d-exp}})\right]\left[\frac{\partial^2 P_{\text{a-void}}}{\partial\rho^2_{\text{d2}}}(\rho_{\text{d-exp}},\rho_{\text{d-exp}})\right]-\left[\frac{\partial^2 P_{\text{a-void}}}{\partial\rho_{\text{d1}}\partial\rho_{\text{d2}}}(\rho_{\text{d-exp}},\rho_{\text{d-exp}})\right]^2$$

$$=\frac{A_1A_2}{AA_3}a_1^2b_1^4\exp^{2b_1\rho_{\text{d-exp}}}>0 \tag{11}$$

and

$$\frac{\partial^2 P_{\text{a-void}}}{\partial\rho^2_{\text{d1}}}(\rho_{\text{d-exp}},\rho_{\text{d-exp}})=\frac{A_1(A_1+A_3)}{AA_3}a_1b_1^2\exp^{b_1\rho_{\text{d-exp}}}>0 \tag{12}$$

Therefore, the function $P_{\text{a-void}}$ has a local minimum at $(\rho_{\text{d-exp}}, \rho_{\text{d-exp}})$ and the local minimum value is $a_1\exp^{b_1\rho_{\text{d-exp}}}$. This means that the global axial swelling pressures of heterogeneous samples are larger than those of homogeneous samples when ρ_{d1}, ρ_{d2} and ρ_{d3} are not equal to $\rho_{\text{d-exp}}$. Moreover, the greater the difference between ρ_{d1}, ρ_{d2}, ρ_{d3} and $\rho_{\text{d-exp}}$, the larger the difference

between the axial swelling pressures of samples with and without voids. This explains the significant difference between the measured axial swelling pressures of the sample with 20% voids and that without voids at the same expected final dry density of 1.6 Mg/m^3.

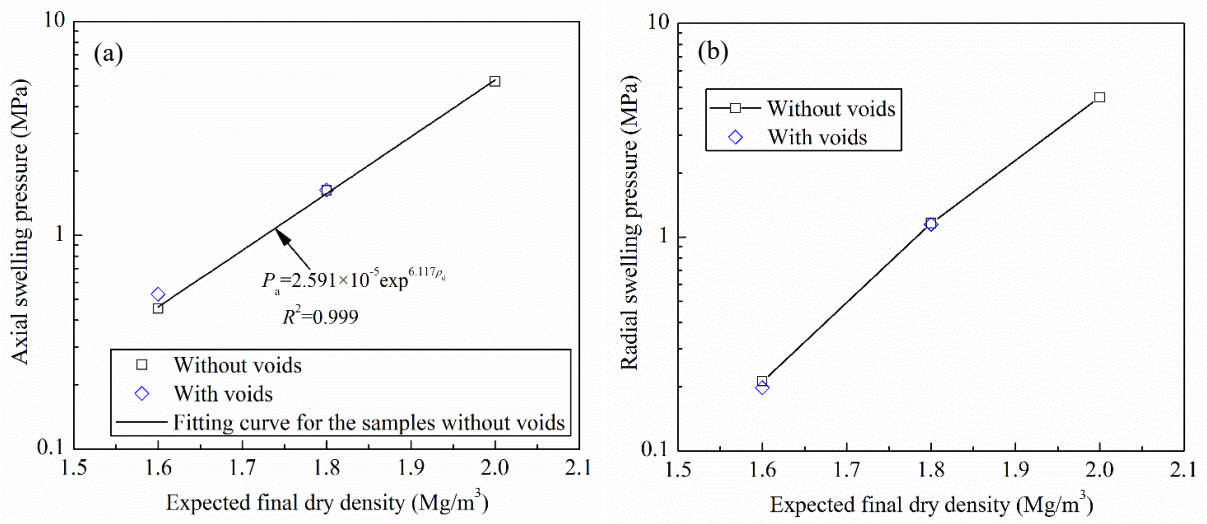

Fig. 16. Relationship between the final swelling pressures and final dry density: (a) axial swelling pressure; (b) radial swelling pressure

Note that the above analytical analysis about the effect of heterogeneity on the axial swelling pressure was preliminary because of the difficulties in the continuous measurement of dry density along the radial direction. Eq. (2) can underestimate the difference of axial swelling pressures between the samples with and without voids, because the dry density distribution of each part was similarly heterogeneous. Based on the measured mean dry densities of parts I, II and III after 2160 h of hydration, the axial swelling pressures of samples with 10 and 20% voids were estimated at 1.58 and 0.50 MPa, respectively. By contrast, the axial swelling pressures of samples without voids at dry densities of 1.8 and 1.6 Mg/m^3 were estimated at 1.57 and 0.46 MPa, respectively. The estimated differences of axial swelling pressures between samples with and without voids are lower than the measured ones, especially for the sample with an expected final dry density of 1.6 Mg/m^3.

As far as the final radial swelling pressure was concerned, a much lower swelling pressure was measured in the radial direction than that in the axial direction, as displayed in Fig. 16b. This aeolotropic behaviour of compacted block could be ascribed to the sample preparation method (Lee et al., 2012; Saba et al., 2014a; Jia et al., 2019). During the uniaxial compaction, the aggregates tended to orientate perpendicular to the compaction direction. Thus, a larger swelling pressure could be expected in the axial direction upon hydration. From Fig. 16b, it could also be observed that the samples with technological voids exhibited a lower radial

swelling pressure than that of the samples without voids, even though the expected final dry density was the same, especially for the sample with 20% voids. For the samples with technological voids, the radial sensor directly measured the local radial pressure of part I (Fig. 2), which corresponded to the initial voids and had a lower dry density than the expected final one (Fig. 9). Additionally, at the heterogeneous stage, the radial swelling of the swelling zone (parts II and III) could be restrained by the friction stress between the filter papers and top and bottom surfaces of samples, resulting in a lower radial pressure sensed at the lateral surface of the samples. These explained why a slightly lower radial swelling pressure was observed for the samples with technological voids.

4.4 Hydraulic conductivity

In addition to the swelling pressure, the hydraulic conductivity is also a key parameter in the design and development of the sealing/backfilling materials. The measured hydraulic conductivities at 2160 h are plotted versus the expected final dry density for all the samples in Fig. 17. In a standard fashion, the hydraulic conductivity of the samples without voids decreased with the increase of dry density and the following relationship between the hydraulic conductivity (k_w in m/s) and the dry density (ρ_d in Mg/m^3) could be derived:

$$k_w=a_2\exp^{b_2\rho_d}=6.761\times10^{-7}\exp^{-6.995\rho_d} \quad (13)$$

where a_2 and b_2 are the fitting parameters. Note that the hydraulic conductivity of samples without voids reached stabilisation after 2160 h of hydration, even though it gradually decreased with time during the first several hundred hours, as reported by Zhu et al. (2013). As mentioned above, the hydraulic conductivity of the samples with technological voids decreased with time and approached that of the samples without voids. This was because part I had a lower dry density, acting as possible preferential flow pathway and facilitated water transfer around the samples and a higher hydraulic conductivity was measured for the samples with technological voids than those without technological voids, at the same expected final dry density. After 2160 h of hydration, the measured hydraulic conductivities of samples with and without initial voids were quite close (Fig. 17). However, owing to the friction between the filter papers and sample, the heterogeneous distribution of dry density could be persistent in the long term (Zeng et al., 2020b) and the hydraulic conductivity could not decrease below that of the samples without voids.

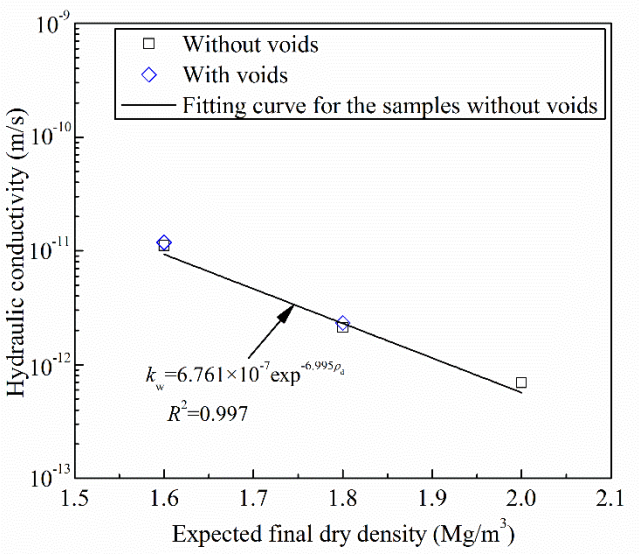

Fig. 17. Relationship between the final hydraulic conductivity and expected final dry density

5 Conclusions

Infiltration tests at different hydration times were performed on compacted bentonite/claystone mixture with various technological voids. The evolutions of axial and radial swelling pressures and hydraulic conductivity with time were investigated, together with the determination of the variations of water content, dry density, suction and microstructure feature at different positions. The results obtained allow the following conclusions to be drawn.

The filling of technological voids led to a sharp decrease in the dry density of soil close to the initial voids and a relatively slow decrease in that far from the voids. After that, a compression zone and a swelling zones could be identified: (i) the compression zone was characterized by a lower dry density than the expected final one; (ii) the swelling zone was represented by a higher dry density than the expected final one. Over time, the soil in the swelling zone underwent further swelling, while that in the compression zone was compressed by the swelling pressure, resulting in a decrease of dry density gradient.

In the compression zone, the global void ratio increased significantly after swelling at the filling stage, with increases in large-pore, medium-pore and inaccessible-pore void ratios but a decrease in small-pore void ratio. Over time, the large and medium pores were compressed by almost constant swelling pressure. By contrast, the volume of large pores of the swelling zone increased until the suction decreased to below 1 MPa and then it decreased from 15 h to 2160 h owing to the water redistribution in the soil. These processes resulted in a relatively uniform microstructure distribution.

After 2160 h of hydration, the water content and dry density distributions of samples with technological voids still remained heterogeneous. Due to this heterogeneity, the samples with initial voids exhibited slightly larger axial swelling pressure and hydraulic conductivity than those without voids at the same expected final dry density; on the contrary, their radial swelling pressure was slightly lower than that of the samples without voids.

Acknowledgments

The authors thank the China Scholarship Council (CSC). The supports provided by Ecole des Ponts ParisTech and the French National Radioactive Waste Management Agency (Andra) are also greatly acknowledged.

References

Alonso, E.E., Romero, E. & Hoffmann, C. (2011). Hydromechanical behaviour of compacted granular expansive mixtures: experimental and constitutive study. Géotechnique 61, No. 4, 329-344.

Bian, X., Cui, Y.J., Zeng, L.L. & Li, X.Z. (2019a). Swelling behavior of compacted bentonite with the presence of rock fracture. Engineering Geology 254, 25-33.

Bian, X., Cui, Y.J. & Li, X.Z. (2019b). Voids effect on the swelling behaviour of compacted bentonite. Géotechnique 69, No. 7, 593-605.

Bian, X., Cui, Y.J., Zeng, L.L. & Li, X.Z. (2020). State of compacted bentonite inside a fractured granite cylinder after infiltration. Applied Clay Science. doi: 10.1016/j.clay.2020.105438

Castellanos, E., Villar, M.V., Romero, E., Lloret, A. & Gens, A. (2008). Chemical impact on the hydro-mechanical behaviour of high-density FEBEX bentonite. Physics and Chemistry of the Earth, Parts A/B/C 33, S516-S526.

Cui, Y. J., Loiseau, C. & Delage, P. (2002). Microstructure changes of a confined swelling soil due to suction controlled hydration. In Unsaturated soils: proceedings of the 3rd international conference on unsaturated soils, UNSAT 2002 (eds J. F. T. Juca, T. M. P. de Campos and F. A. M. Marinho), vol. 2, pp. 593–598. Lisse, the Netherlands: Balkema.

Cuisinier, O., Masrouri, F., Pelletier, M., Villieras, F. & MosserRuck, R. (2008). Microstructure of a compacted soil submitted to an alkaline plume. Appl. Clay Sci. 40, No. 1–4, 159–170.

Delage, P., Marcial, D., Cui, Y.J. & Ruiz, X. (2006). Ageing effects in a compacted bentonite: a microstructure approach. Géotechnique 56, No. 5, 291-304.

Fouché, O., Wright, H., Le Cléac'h, J.M. & Pellenard, P. (2004). Fabric control on strain and rupture of heterogeneous shale samples by using a non-conventional mechanical test.

Applied Clay Science 26, No. 1-4, 367-387.

Gatabin, C., Talandier, J., Collin, F., Charlier, R. & Dieudonné, A.C. (2016). Competing effects of volume change and water uptake on the water retention behaviour of a compacted MX-80 bentonite/sand mixture. Applied Clay Science 121, 57-62.

Gens, A., Vállejan, B., Sánchez, M., Imbert, C., Villar, M. V. & Van Geetl, M. (2011). Hydromechanical behaviour of a heterogeneous compacted soil: experimental observations and modelling. Géotechnique 61, No. 5, 367-386.

Jia, L.Y., Chen, Y.G., Ye, W.M. & Cui, Y.J. (2019). Effects of a simulated gap on anisotropic swelling pressure of compacted GMZ bentonite. Engineering Geology 248, 155-163.

Kiviranta, L. & Kumpulainen, S. (2011). Quality control and characterization of bentonite materials, Posiva Working Report 2011-84. Olkiluoto, Eurajoki, Finland: Posiva Oy. See https://www.posiva.fi/files/1994/WR_2011-84_web.pdf

Lee, J.O., Lim, J.G., Kang, I.M. & Kwon, S. (2012). Swelling pressures of compacted Ca-bentonite. Engineering Geology 129, 20-26.

Martin, P.L., Barcala, J.M. & Huertas, F. (2006). Large-scale and long-term coupled thermo-hydro-mechanic experiments with bentonite: the FEBEX mock-up test. J. Iberian Geol. 32, No. 2, 259-282

Mokni, N., Barnichon, J.D., Dick, P. & Nguyen, T.S. (2016). Effect of technological macro voids on the performance of compacted bentonite/sand seals for deep geological repositories. International Journal of Rock Mechanics and Mining Sciences 88, 87-97.

Saba, S., Delage, P., Lenoir, N., Cui, Y.J., Tang, A.M. & Barnichon, J.D. (2014a). Further insight into the microstructure of compacted bentonite–sand mixture. Engineering geology 168, 141-148.

Saba, S., Barnichon, J.D., Cui, Y.J., Tang, A.M. & Delage, P. (2014b). Microstructure and anisotropic swelling behaviour of compacted bentonite/sand mixture. Journal of Rock Mechanics and Geotechnical Engineering 6, No. 2, 126-132.

Saba, S., Cui, Y.J., Tang, A.M. & Barnichon, J.D. (2014c). Investigation of the swelling behaviour of compacted bentonite–sand mixture by mock-up tests. Canadian Geotechnical Journal 51, No. 12, 1399-1412.

Saiyouri, N., Hicher, P. & Tessier, D. (1998). Microstructural analysis of highly compacted clay swelling. In Proceedings of the 2nd international conference on unsaturated soils, vol. 1, pp. 119–124. Beijing, China: International Academic Publisher.

Saiyouri, N., Hicher, P.Y. & Tessier, D. (2000). Microstructural approach and transfer water modelling in highly compacted unsaturated swelling clays. Mechanics of Cohesive-frictional Materials: An International Journal on Experiments, Modelling and Computation of Materials and Structures 5, No. 1, 41-60.

Villar, M.V., García-Siñeriz, J.L., Bárcena, I. & Lloret, A. (2005). State of the bentonite barrier

after five years operation of an in situ test simulating a high level radioactive waste repository. Engineering Geology 80, No. 3-4, 175-198.

Villar, M.V. & Lloret, A. (2008). Influence of dry density and water content on the swelling of a compacted bentonite. Applied Clay Science 39, No. 1-2, 38-49.

Wang, Q., Tang, A.M., Cui, Y.J., Delage, P., Barnichon, J.D. & Ye, W.M. (2013a). The effects of technological voids on the hydro-mechanical behaviour of compacted bentonite–sand mixture. Soils and Foundations 53, No. 2, 232-245.

Wang, Q., Cui, Y.J., Tang, A.M., Barnichon, J.D., Saba, S. & Ye, W.M. (2013b). Hydraulic conductivity and microstructure changes of compacted bentonite/sand mixture during hydration. Engineering Geology 164, 67-76.

Wang, Q., Cui, Y.J., Tang, A.M., Li., X.L. & Ye, W.M. (2014). Time-and density-dependent microstructure features of compacted bentonite. Soils and Foundations 54, NO. 4, 657-666.

Ye, W.M., Lai, X.L., Liu, Y., Chen, Y.G. & Cui, Y.J. (2013). Ageing effects on swelling behaviour of compacted GMZ01 bentonite. Nuclear Engineering and Design 265, 262-268.

Zeng, L.L., Cui, Y.J., Conil, N., Zghondi, J., Armand, G. & Talandier, J. (2016). Experimental study on swelling behaviour and microstructure changes of natural stiff Teguline clays upon wetting. Canadian Geotechnical Journal 54, No. 5, 700-709.

Zeng, Z.X., Cui, Y.J., Zhang, F., Conil, N. & Talandier, J. (2019). Investigation of swelling pressure of bentonite/claystone mixture in the full range of bentonite fraction. Applied Clay Science. doi: 10.1016/j.clay.2019.105137.

Zeng, Z.X., Cui, Y.J., Zhang, F., Conil, N. & Talandier, J. (2020a). Effect of technological voids on the swelling behaviour of compacted bentonite/claystone mixture. Canadian Geotechnical Journal. doi: 10.1139/cgj-2019-0339.

Zeng, Z.X., Cui, Y.J, Conil, N. & Talandier J. (2020b). Analysis of boundary friction effect on the homogenization process of compacted bentonite/claystone mixture with technological voids upon hydration. Acta Geotech., in press, https://doi.org/10.1007/s11440-020-01048-x.

Zhu, C.M., Ye, W.M., Chen, Y.G., Chen, B. & Cui, Y.J. (2013). Influence of salt solutions on the swelling pressure and hydraulic conductivity of compacted GMZ01 bentonite. Engineering Geology 166, 74-80.